Characterizing mineral wettabilities on a microscale by colloidal probe atomic force microscopy

Babel, B. M.; Rudolph, M.;

Originally published:

March 2018

Minerals Engineering 121(2018), 212-219

DOI: https://doi.org/10.1016/j.mineng.2018.02.003

Characterizing mineral wettabilities on a microscale by colloidal probe atomic force microscopy

Bent Babel, Martin Rudolph

Helmholtz Institute Freiberg for Resource Technology, Helmholtz-Zentrum Dresden-Rossendorf, Chemnitzer Straße 40, 09599 Freiberg, Germany

b.babel@hzdr.de

Abstract

For finely intergrown ores the characterization of reagent-mineral interactions in flotation systems holds difficult challenges for the applicability of standard techniques like hallimond tube tests or contact angle experiments or renders them impossible while other techniques might not work in an aqueous environment. We present the utilization of an atomic force microscope with a hydrophobic colloidal probe to characterize the wettabilities of individual mineral grains on a microscale. The sulfidic ore sample containing chalcopyrite, pyrite and quartz is investigated in an aqueous environment. The mineralogy of the sample is characterized by SEM+EDX and its wettability by contact angle measurements. Force mappings on the respective minerals are performed and allow a distinction between quartz, chalcopyrite and pyrite with the resulting force distributions. An additional focus in this paper lies on the heterogeneities within one mineral surface domain and the applicability for grain mappings.

Highlights:

- the hydrophobic interaction was used to characterize the wettabillites of mineral surface domains allowing a distinction between sulfidic minerals and quartz
- adhesion / hydrophobic imaging was used to visualize varying degrees of hydrophobicity on mineral grains
- limitations are given by probe degradation and topographic inhomogeneities

Keywords:

hydrophobic interaction, atomic force microscopy, wettabilities, adhesion imaging, flotation

1. Introduction

As the process result in flotation is to a great extend governed by the wettabilities of the involved particle systems it is crucial to have an understanding of particle – reagent interactions. For finely intergrown ores the characterization of these interactions holds difficult challenges for the applicability of standard techniques like hallimond tube tests or contact angle experiments by the availability of suitable sample material in quantity and quality. For more sophisticated techniques like XPS, AES, vibrational spectroscopy and SIMS limitations are given by the measurement conditions.

Therefore there is a need to develop a technique able to characterize mineral wettabilites in an aqueous environment with a high spatial resolution. In 2014 Rudolph and Peuker [1, 2] described

Abbreviations: XPS X-ray photoelectron spectroscopy, AES Auger electron spectroscopy, SIMS secondary ion mass spectroscopy, SEM scanning electron microscope, EDX energy dispersive X-ray spectroscopy, AFM atomic force microscope, CP-AFM colloidal probe atomic force microscopy , SD standard deviation, ROI region of interest

the application of an atomic force microscope (AFM) utilizing a polystyrene probe to measure force interactions on polished mineral samples with different measuring modes. A similar concept was also applied by Xie et al. using a hydrophobized conventional cantilever to probe the nanoscale hydrophobicity on a sphalerite surface [3] and Wada et al. who used the colloidal probe AFM (CP-AFM) technique to probe the local hydrophobicity of a sapphire surface [4].

This paper aims to critically display the advantages and limitations of the CP-AFM technique to characterize the wettabilities of mineral surfaces. The term hydrophobic will be used in the context of froth flotation, i.e. when a particle is able to attach to a gas bubble and not by its classical definition, i.e. the water contact angle is larger than 90°, although it is handled differently in the literature cited. The technique presented in this paper utilizes the concept of hydrophobic interactions, which has been extensively studied over the past decades by various research groups and was first reported by Blake and Kitchener [5]. Described as a long-range attractive interaction the adhesive forces associated are about an order of magnitude higher than maximum possible van der Waals dispersion forces. Israelachvili and Pashley suggested that the interaction might be related to the local water structure at solid-liquid interfaces [6]. Parker et al. concluded that the long-ranged attraction between hydrophobic surfaces most likely originates from submicroscopic bridging bubbles or cavities [7], while this mechanism was being questioned due to the lifetime of nanoscopic bubbles in water ranging from 1 µs to 100 µs for bubble radii of 10 nm to 100 nm due to their Laplace pressure [8]. A variety of sources for the interactions were discussed in a review by Attard [9].

Today nanobubbles are widely accepted as the cause for the long range attractive interaction (5 – 275 nm) [10], as they were imaged by AFM based techniques and additional methods [11-13]. Detecting heights and shapes the authors described these gas domains either as isolated [13], networks [11] or as micropancakes [14] which gives an indication for the extreme variability in the range of the measured forces due to variability in the coverage and size of such nanobubbles [9].

Mechanisms of nanobubble formation are the supersaturation of the solvent [13] e.g. by addition of ethanol in water, temperature change [7], submersion of a hydrophobic and or rough surface and formation of nanobubbles in the contact region of hydrophobic surfaces [7, 15]. Therefore the range of the attraction is governed by the aeration state of the solvent leading to shorter attraction distances in degassed water [9]. Yang et al. investigated surfaces with a different degree of surface hydrophobicity and nanoscale roughness concluding that the bubbles formed on rough surfaces were larger and less densely distributed than those on a smooth surface of similar hydrophobicity [13]. This should lead to broader distributed values in force spectroscopic measurements in terms of long range attraction und maximum adhesion. Contradicting results were published by Wallquist [15]. For more detailed information on nanobubbles refer to the reviews compiled by Attard and Hampton [9, 16].

In the last years, in contrast to the beginning of the research on nanobubbles, the focus shifted from investigating the hydrophobic effect itself to utilizing it to characterize the wettabilities of solid-liquid interfaces on AFM based techniques [1-4, 17-20]. Force spectroscopic imaging has so far been published by multiple authors in a biological context [21, 22], with functionalized silica surfaces of varying roughness [15] and by probing a sphalerite surface [3], but to the best knowledge of the author was yet not reported on a natural ore section with varying wettabilities.

2. Materials and methods

2.1 Chemicals

HCl, NaOH, KCl and ethanol (ROTISOLV® HPLC Gradient Grade), which were used to prepare the background solution, for pH adjustment and sample cleaning, were supplied by Carl Roth GmbH and used as received. K-octylxanthate was used to hydrophobize the sulfidic minerals and DYNASYLAN® F8261 for the colloidal probes and the reference sample. For the preparation of the colloidal probes epoxy glue (Uhu Plus Endfest 300) was utilized and the polishing of the substrate was performend with DiaPro ¼ µm diamond suspension by Struers.

2.2 Colloidal probe preparation

Colloidal probe cantilevers were prepared by gluing 19.59 (+-) 0,69 µm spherical and smooth SiO_2 particles (microparticles GmbH) onto All-In-One B and C type cantilevers (nano and more GmbH) after determining their resonance frequency for force constant calibration described in [23]. After setting of the glue the probes were plasma cleaned to remove organic contamination and to provide a high surface density of OH groups. Subsequently the probes and a similarly cleaned glass slide were functionalized by a procedure adapted from Hozumi et al. [24]. The parameters were set to 2 h at 115 °C with 50 µl DYNASYLAN® F8261. The result of the silanization was checked by contact angle measurements. An overview of the used cantilevers and probes is provided in Table 1.

Table 1: *Cantilever properties, * indicates a cantilever reequipped with a new SiO_2 particle*

cantilever	probe	force constant in N/m	application
1	CP1	2.16	force distributions
2	CP2	2.07	force distributions
3	CP3	2.01	force distributions
4	CP4	2.18	force distributions
5	CP5	2.01	force distributions
6	CP6	2.22	force distributions
1*	CP7	2.07	grain mapping
2*	CP8	2.01	grain mapping
7	CP9	5.79	reference sample

2.3 Sample characterization and regions of interest

The sample consists of a sulfidic ore section embedded in an epoxy resin gradually machine polished and finished by the procedure described in 2.4. The mineralogical composition of the sample was characterized by automated mineralogy, i.e. SEM+EDX and the main minerals are chalcopyrite, pyrite and quartz. The size of the mineral domains is sufficient to allow a macroscopic wettability characterization by sessile drop contact angle measurements. For the microscopic investigations three regions of interest (ROI) were defined as displayed in Fig.1.

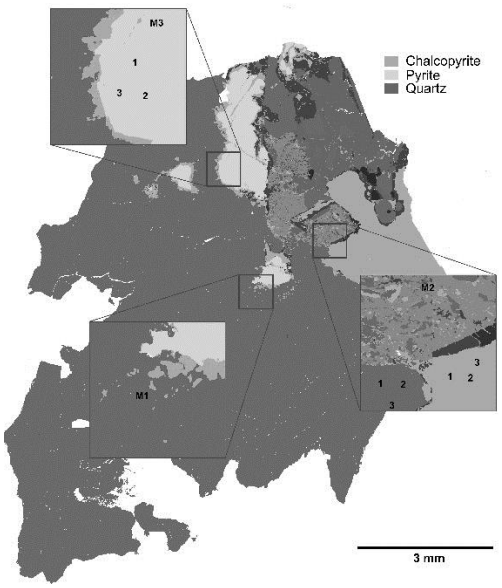

Fig.1: *SEM+EDX based picture with highlighted ROIs. Numbers indicate the mapped areas per mineral and M1-M3 indicate the grain mapping areas.*

2.4 Sample preparation

As sulfides tend to oxidize altering their surface properties, prior to the contact angle and AFM measurements the sample was polished with a diamond suspension on a DP-Nap polishing cloth also supplied by Struers. Following this step the sample was cleaned in a beaker with KCl solution in an ultrasonic bath, rinsed by ethanol and swiped with a lint free cloth. Finally the sample was sonicated for 5 minutes in DI water to ensure the removal of residual ethanol. The author is aware that this procedure might already be changing the surface properties of the minerals and therefore the results obtained in this study might not reflect their known process behavior. To account for a possible alteration the adsorption behavior of K-octylxanthate was verified. Therefore the sample was submerged in 50 ml KCl solution set to pH 7 for 5 minutes. After 2.5 minutes the K-octylxanthate stock solution was added setting the concentration to 10^{-6} M. During conditioning the solution was stirred with a magnetic stirrer and the pH adjusted if necessary. In addition to the natural ore sample contact angles and adhesion forces were measured on a hydrophobized glass slide for reference values.

2.5 Contact angle measurements

Contact angle measurements were performed with an electronic dosing system of a DataPhysics OCA 50 and deionized water. Prior to the initial measurement the surfaces were cleaned by the polishing procedure described in 2.4. For each subsequent time dependent measurement the sample was covered by 1 ml KCl solution set to pH 7 reflecting the measurement conditions in the AFM to observe possible surface alteration. As described by Raichur et al. the oxidation rate in water is minimal in neutral pH range for pyrite [25]. For each data point at least 3 measurements were averaged.

2.6 Atomic force microscopy

The atomic force microscope measurements were carried out with a Park Systems XE100. The sample roughness was characterized in non-contact mode on 20 µm x 20 µm, scanning three areas per ROI with a TAP 300 Al-G cantilever (nano and more GmbH). The force distance curves were gathered 10 minutes after the sample was submerged in 1 ml 10^{-2} M KCl solution at pH 7 in a tempered liquid cell at 20 °C and immediate immersion of the colloidal probe. For this study only the unconditioned sample state was investigated via AFM. The data gathered was processed with a matlab script designed by Dr.-Ing. Jörg Fritzsche and the snap in distance and maximum adhesion force are discussed in this study. The mapping areas for mono mineral domains were set to 20 µm x 20 µm with 64 points measured and two sets of three different colloidal probes were interchanged for the minerals to reduce the influence of probe degradation and variation. The grain mappings were adapted to the grain size and performed with 256 points per grain utilizing two additional colloidal probes. The total times per mapping were about 10 minutes and 40 minutes for mono minerals and grain mappings respectively. The forces limit was kept constant at 100 nN and the z-scanner speed was set to 1 µm/s.

3. Results and discussion

3.1 Contact Angle measurements

The results of the contact angle measurements are displayed in Fig. 2. For the unconditioned sample only minor shifts in the average contact angel can be noted for chalcopyrite and pyrite. The conditioned samples are plotted with 5 minutes delay accounting for the conditioning step. For the initial state of the CP-AFM measurements the contact angles for the minerals chalcopyrite, pyrite and quartz are 68°, 52° and 12° respectively. The change in contact angle with addition of K-octylxanthate indicates that the unconditioned surfaces reflect the natural state of the mineral surfaces. The measurements of the reference sample (glass slide) conditioned with the silane resulted in an average contact angle of 106° indicating a monolayer coverage [24].

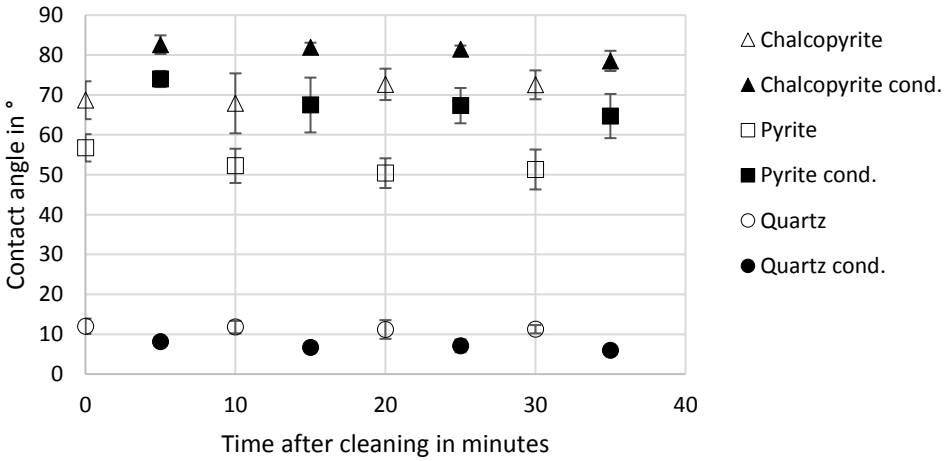

Fig. 2: *Time dependent contact angles and their standard deviations with and without K-octylxanthate*

3.2 Roughness measurements

The results of the roughness measurements are given in the root-mean-squared (rms) roughness and are summarized in Table 2. The values acquired on 20 µm x 20 µm on at least five areas per ROI correlate well with the Mohs hardness of the minerals given in [26]. As described in the first section the nano scale roughness of the sample plays a crucial role in the size and distribution of nanobubbles at the solid-liquid interface. Therefore the roughness has to be taken into account to evaluate the resulting force distributions.

Table 2: *rms roughness and Mohs hardness data for the minerals investigated and the reference sample*

sample	rms in nm	SD rms	Mohs hardness
chalcopyrite	1.12	0.04	3.5 - 4
pyrite	0.51	0.01	6 - 6.5
quartz	0.38	0.06	7
ref. sample	2.08	0.69	x

3.3 CP-AFM mono mineral domains

The results of the CP-AFM investigations on the mono mineral domains are plotted in Fig. 3 as cumulative distributions of maximum adhesion forces normalized on the particle radius of each point measured for chalcopyrite, pyrite, quartz and the reference sample.

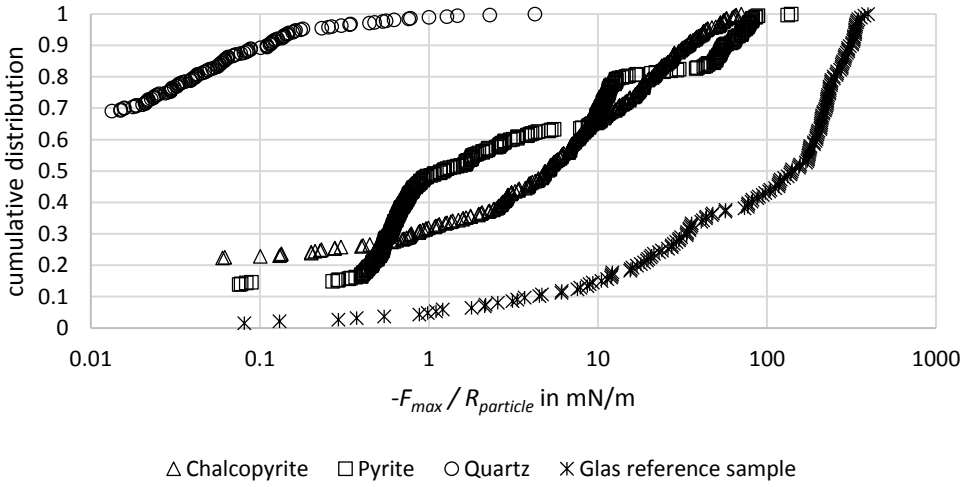

Fig. 3 *Cumulative force distributions*

The median values for the $-F_{max} / R_{particle}$ distributions for chalcopyrite, pyrite and the reference sample are 4.9 mN/m, 1.2 mN/m and 140 mN/m, respectively, while the median for quartz is 0. The overall order of median values fits the order in macroscopic contact angles. A distinction between quartz and both chalcopyrite and pyrite is possible by the display of the cumulative distribution of measured forces. The comparison between the cumulative distributions of chalcopyrite and pyrite shows that pyrite has the lower median, despite having higher maximum values. The distribution of forces for pyrite shows three steps in its progression originating from relatively homogeneous force mappings. This might be related to the smoother surface of pyrite which would result in a more homogeneous distribution of nanobubbles [13]. The resulting distributions are relatively broad even for the assumed monolayer of the reference sample. This

might be related to a gradual degradation of the colloidal probe, non-hydrophobic surface sites, irregular nanobubble distribution, unfavorable contact geometries and possible contamination by polishing media for the polished sample and surface alteration in the case of sulfidic surfaces.

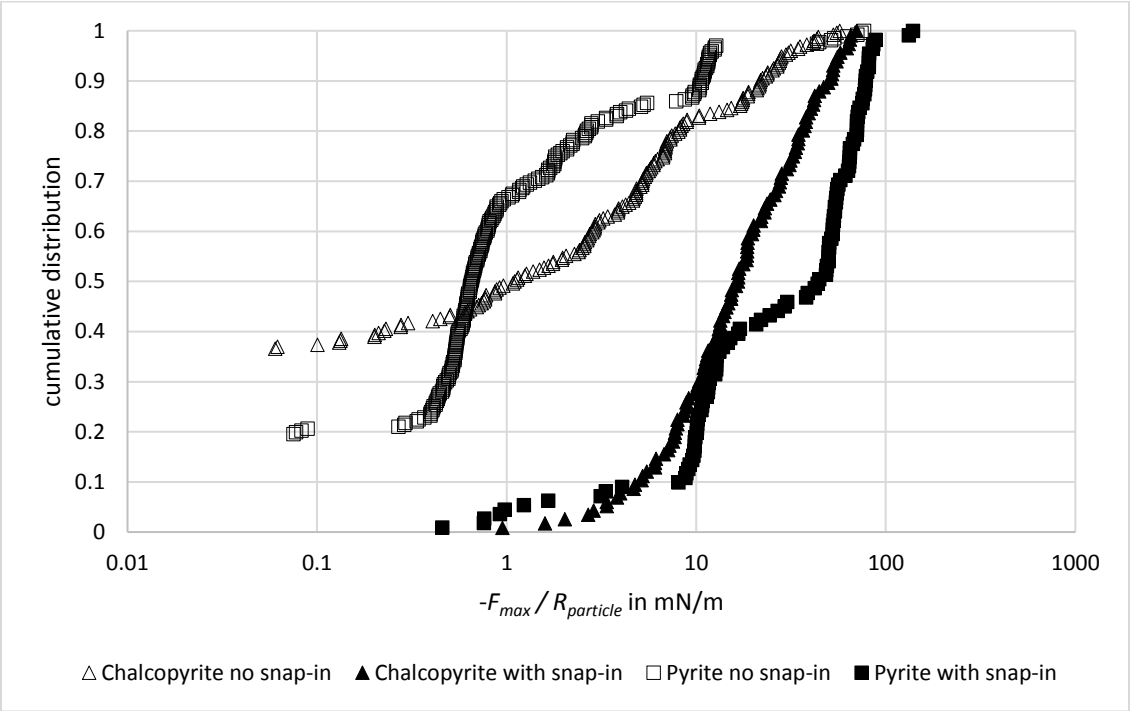

***Fig. 4**: Filtered cumulative force distributions for chalcopyrite and pyrite including and excluding snap in events in the force distance curves*

In Fig. 4 the cumulative force distribution data is filtered for force distance curves with a snap-in and without a snap-in event in the approach for chalcopyrite and pyrite, indicating different adhesion mechanisms. The adhesion forces with a snap-in event are assumed to be caused by preexisting nanobubbles on the interacting surfaces. The ones without prior snap-in events are expected to be induced by the formation of nanobubbles through gas nucleation in the contact area. The force distributions with snap in events show a trend towards higher adhesive forces for both minerals while the median values are 16.6 mN/m and 1.1 mN/m for chalcopyrite and 44.7 mN/m and 0.7 mN/m for pyrite with and without a snap-in respectively. As described in the first section the formation of nanobubbles between hydrophobic surfaces is possible and an explanation for the force distributions with no snap-in events. The maximum forces of the distributions for chalcopyrite with and without snap in events are in the same order of magnitude, while they differ for pyrite by about one order of magnitude. The overall lower distribution of values might be related to the limited contact time for the nucleation of gas and formation of a gas capillary and by surface sites with an overall lower hydrophobicity. The component responsible for the nucleation of a gas capillary between the probe and the sample seems to be lower for pyrite, while the preexisting nanobubbles on pyrite seem to lead to a higher adhesion, even with displaying a lower median for snap-in distances (see Fig. 5).

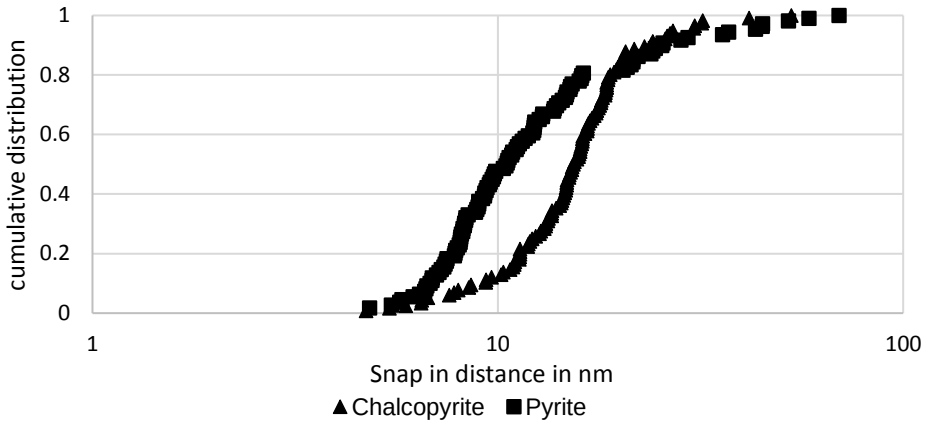

Fig. 5: *Cumulative snap in distance distributions*

Fig. 5 shows the cumulative snap-in distance distribution for chalcopyrite and pyrite. The values are more broadly distributed for pyrite with a maximum value of 70 nm and a median of 10.5 nm compared to 53 nm and 15.4 nm for chalcopyrite. Concluding that the pyrite surface with a macroscopic contact angle of 52° and a lower surface roughness is displaying broader adhesion force and snap-in distance distributions while having overall lower median values compared to chalcopyrite. This result is not consistent with trends described in literature for the size of nanobubbles on hydrophobic surfaces with varying degree of roughness [13]. A possible explanation might be a heterogeneous oxidation behavior of pyrite. The higher maxima might be explained by a trend described in section 3.4 shown in Fig. 10. Nevertheless the surfaces investigated in this study are natural minerals of an ore section and hardly comparable to well defined sample surfaces of most previous investigations which is unique for this study.

3.4 CP-AFM grain mappings

As described before within the analysis of the maximum adhesion forces a distinction between the sulfidic minerals and quartz as hydrophobic and hydrophilic surfaces can be achieved, while the distinction between chalcopyrite and pyrite is more challenging. Three ROIs were chosen to test the applicability of grain mappings displaying chalcopyrite grains in spatial resolved pictures of adhesive forces or snap-in distances. Force distance curves which could not be processed by the matlab script are marked as hatched areas. The grain mappings M1 and M2 are displayed in Fig. 6 and Fig. 7 showing a chalcopyrite grain in a matrix consisting of epidote and orthoclase and a chalcopyrite grain in quartz. These mapped forces are not included in the cumulative force distributions of section 3.3, while they are partially displaying higher maximum adhesion forces up to 160 mN/m.

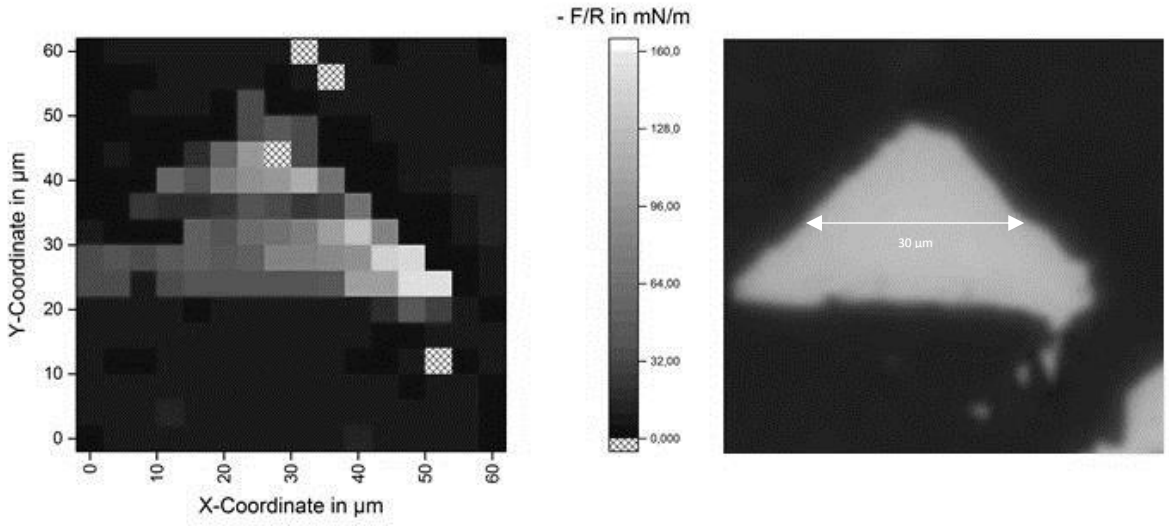

Fig. 6: *M1 adhesion mapping and microscope image (AFM top CCD camera) of a chalcopyrite grain in quartz (note unequal spatial scaling for left and right images)*

The mappings M1 and M2 show a clear distinction between chalcopyrite and the surrounding mineral phases. The distribution of adhesive forces is rather homogeneous for M2, while M1 shows a trend to higher adhesive force to the lower right edges of the grain and a broader overall distribution. This might be related to a gap (see Fig. 9 between 65 µm – 70 µm) at the grain boundary and or different contact geometries caused by the height difference at the transition to the quartz areas.

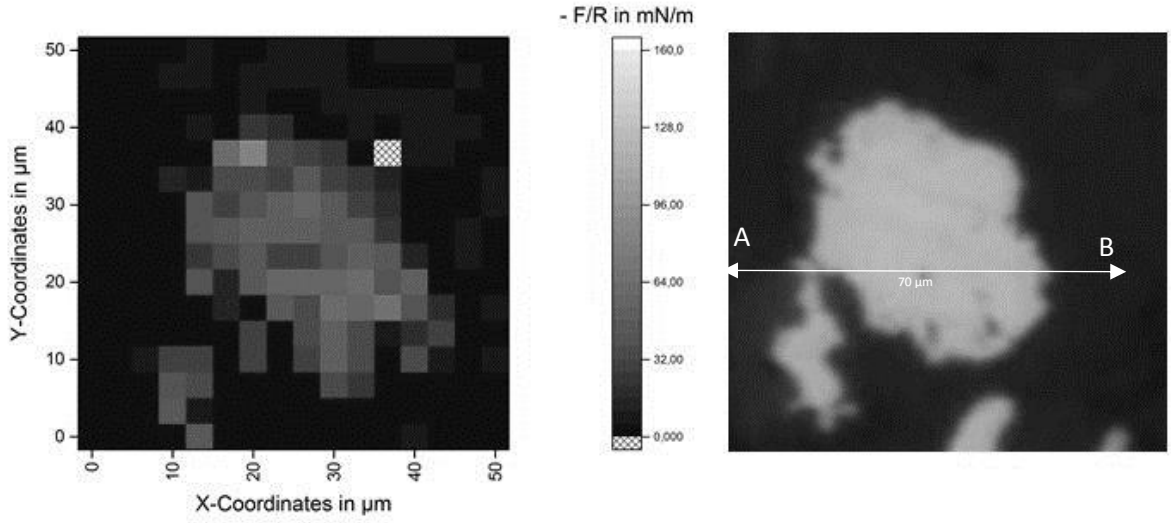

Fig. 7: *M2 adhesion mapping and microscope image (AFM top CCS camera) of a chalcopyrite grain in epidote and orthoclase (note unequal spatial scaling for left and right images)*

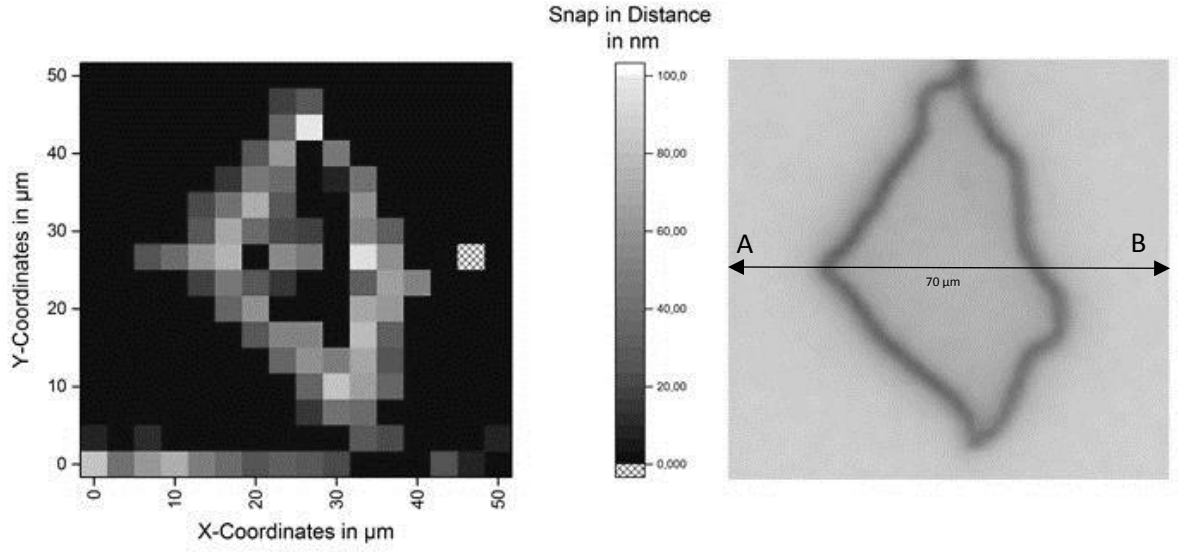

Fig. 8: *M3 mapping plotted as snap-in distance and microscope image (AFM top CCD camera) of a chalcopyrite grain in pyrite (note unequal spatial scaling for left and right images)*

Fig. 8 shows a snap-in distance mapping of a chalcopyrite grain in a pyrite matrix and the associated microscopic image. The first measurements in the bottom row show high initial snap-in distances most likely caused by initial nanobubble(s) at the surface of the hydrophobic colloidal probe, while the latter snap-in events represent either nanobubbles at the mineral surfaces and/or nanobubbles reformed during contact or different contact geometries due to the height profile of the grain. The spatial distribution of snap-in distances located at the edges of the grain is emphasizing the relevance of surface inhomogeneities in terms of the actual grain boundary and changes in contact geometry as shown in Fig. 9 displaying the cross sections A-B of mapping M2 and M3. This observation seems to be only relevant for boundaries with two at least moderately hydrophobic surfaces, as this effect is not visible in M1 and M2.

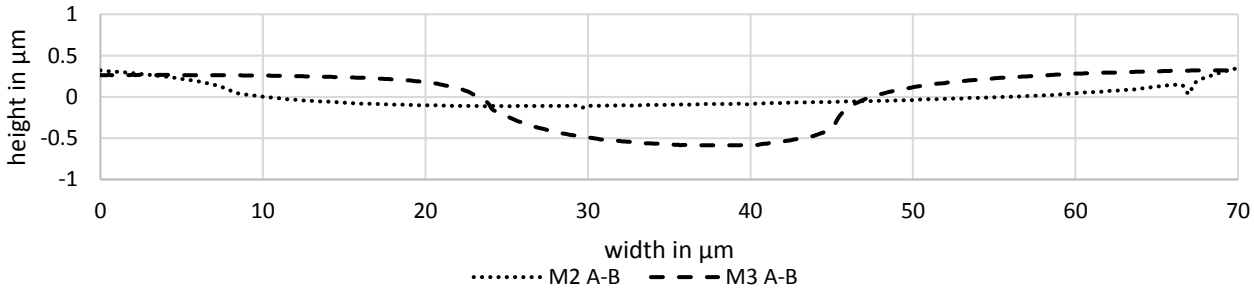

Fig. 9: *Cross sections A-B with a non-isometric scaling for Mapping M2 and M3*

In Fig. 10 the relation between snap-in distance and max adhesion force for the first 16 measured points of mapping M3 is plotted, following a quasilinear trend. A similar trend was reported by Rudolph and Peuker [2]. This relation was appearing randomly in the whole test work and only holds true for the initial measurements of a mapping. This is indicating that the behavior is related to nanobubbles in the contact area of the colloidal probe. As hydrophobic surfaces tend to display nanobubbles it is comprehensible that the colloidal probe entering the system is also covered by an initial volume of nanobubbles in the contact area. For the initial measurements the interaction

is thus supposedly mainly governed by the capillary of initial nanobubbles, while the rest of the snap in events is either caused by nanobubbles on the mineral surfaces or nanobubbles from a previous contact.

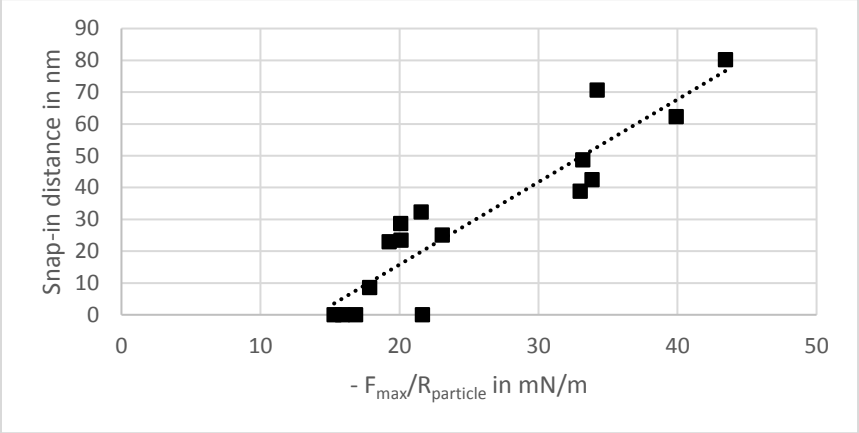

Fig. 10: *Relation of snap-in distance to - $F_{max}/R_{particle}$ in mN/m for the bottom row of M3 (measurement 1-16)*

4. Conclusions and outlook

With respect to previous investigations on mostly well-defined chemically and topographically homogeneous surfaces the CP-AFM technique proofed its value for investigating the wettability of minerals in ore sections on a micro scale. Two measuring concepts were presented either mappings on mono mineral surface domains and comparison of force distributions or grain mappings directly contrasting adhesive forces of the underlying surfaces. The comparison of adhesive force distributions shows a shift to higher adhesive forces with an increase in the macroscopic contact angle, also discussing different adhesion mechanisms. While the discriminability between chalcopyrite and quartz by contact angle is clearly reflected by the force distribution relation, the distinction between chalcopyrite and pyrite with a difference in contact angle of about 15°, is yet more difficult to discuss due to the broader distribution of adhesive forces and snap-in distances for pyrite.

The direct relation of adhesive forces in grain mappings has advantages for comparability, as the colloidal probe has a similar degree of wear, but for the grain boundary area the forces might not reflect the forces on mono mineral surface domains as they are falsified by more favorable contact geometries and the possible formation of nanobubbles at surface inhomogeneities. Therefore to put the measured forces in perspective, a good knowledge of the underlying topography is crucial. Further challenges which will have to be addressed are improvement of the sample preparation step and cleaning procedures in terms of reducing the deviation of surface roughness between mineral phases, sample and probe contamination by residual polishing media.

The next step will be the application of collector molecules to alter the wettabilities of mineral phases and the resulting shifts in force distributions. An additional focus will lie on the establishment of co-localised AFM-Raman measurements and finally a correlation of the gathered data with standard techniques like contact angle and hallimond tube experiments.

This research was funded by the POF III (project oriented funding) of the Helmholtz Foundation designated for Flotation Research in the EMR program under subtopic 5 (resource technologies).

References

1. Rudolph, M. and U.A. Peuker, *Hydrophobicity of Minerals Determined by Atomic Force Microscopy – A Tool for Flotation Research.* Chemie Ingenieur Technik, 2014. **86**(6): p. 865-873.
2. Rudolph, M. and U.A. Peuker, *Mapping hydrophobicity combining AFM and Raman spectroscopy.* Minerals Engineering, 2014. **66**: p. 181-190.
3. Xie, L., et al., *Mapping the Nanoscale Heterogeneity of Surface Hydrophobicity on the Sphalerite Mineral.* The Journal of Physical Chemistry C, 2017. **121**(10): p. 5620-5628.
4. Wada, T., et al., *Characterization of local hydrophobicity on sapphire (0001) surfaces in aqueous environment by colloidal probe atomic force microscopy.* Applied Surface Science, 2017. **396**: p. 1206-1211.
5. Blake, T.D. and J.A. Kitchener, *Stability of aqueous films on hydrophobic methylated silica.* Journal of the Chemical Society, Faraday Transactions 1: Physical Chemistry in Condensed Phases, 1972. **68**(0): p. 1435-1442.
6. Israelachvili, J. and R. Pashley, *The hydrophobic interaction is long range, decaying exponentially with distance.* Nature, 1982. **300**(5890): p. 341-342.
7. Parker, J.L., P.M. Claesson, and P. Attard, *Bubbles, cavities, and the long-ranged attraction between hydrophobic surfaces.* The Journal of Physical Chemistry, 1994. **98**(34): p. 8468-8480.
8. Ljunggren, S. and J.C. Eriksson, *The lifetime of a colloid-sized gas bubble in water and the cause of the hydrophobic attraction.* Colloids and Surfaces A: Physicochemical and Engineering Aspects, 1997. **129**: p. 151-155.
9. Attard, P., *Nanobubbles and the hydrophobic attraction.* Advances in Colloid and Interface Science, 2003. **104**(1): p. 75-91.
10. Yakubov, G.E., H.-J. Butt, and O.I. Vinogradova, *Interaction Forces between Hydrophobic Surfaces. Attractive Jump as an Indication of Formation of "Stable" Submicrocavities.* The Journal of Physical Chemistry B, 2000. **104**(15): p. 3407-3410.
11. Switkes, M. and J.W. Ruberti, *Rapid cryofixation/freeze fracture for the study of nanobubbles at solid–liquid interfaces.* Applied Physics Letters, 2004. **84**(23): p. 4759-4761.
12. Zhang, X.H., A. Quinn, and W.A. Ducker, *Nanobubbles at the interface between water and a hydrophobic solid.* Langmuir, 2008. **24**(9): p. 4756-64.
13. Yang, J., et al., *Very Small Bubble Formation at the Solid−Water Interface.* The Journal of Physical Chemistry B, 2003. **107**(25): p. 6139-6147.
14. Seddon, J.R. and D. Lohse, *Nanobubbles and micropancakes: gaseous domains on immersed substrates.* J Phys Condens Matter, 2011. **23**(13): p. 133001.
15. Wallqvist, V., et al., *Influence of Surface Topography on Adhesive and Long-Range Capillary Forces between Hydrophobic Surfaces in Water.* Langmuir, 2009. **25**(16): p. 9197-9207.
16. Hampton, M.A. and A.V. Nguyen, *Nanobubbles and the nanobubble bridging capillary force.* Advances in Colloid and Interface Science, 2010. **154**(1): p. 30-55.
17. Ditscherlein, L., J. Fritzsche, and U.A. Peuker, *Study of nanobubbles on hydrophilic and hydrophobic alumina surfaces.* Colloids and Surfaces A: Physicochemical and Engineering Aspects, 2016. **497**: p. 242-250.

18. Fritzsche, J. and U.A. Peuker, *Particle adhesion on highly rough hydrophobic surfaces: The distribution of interaction mechanisms.* Colloids and Surfaces A: Physicochemical and Engineering Aspects, 2014. **459**: p. 166-171.
19. Fritzsche, J. and U.A. Peuker, *Wetting and Adhesive Forces on Rough Surfaces – An Experimental and Theoretical Study.* Procedia Engineering. **102**: p. 45-53.
20. Wallqvist, V., et al., *Interaction forces between talc and hydrophobic particles probed by AFM.* Colloids and Surfaces A: Physicochemical and Engineering Aspects, 2006. **277**(1): p. 183-190.
21. Willemsen, O.H., et al., *Simultaneous height and adhesion imaging of antibody-antigen interactions by atomic force microscopy.* Biophysical Journal, 1998. **75**(5): p. 2220-2228.
22. Sullan, R.M.A., J.K. Li, and S. Zou, *Direct Correlation of Structures and Nanomechanical Properties of Multicomponent Lipid Bilayers.* Langmuir, 2009. **25**(13): p. 7471-7477.
23. Butt, H.-J., B. Cappella, and M. Kappl, *Force measurements with the atomic force microscope: Technique, interpretation and applications.* Surface Science Reports, 2005. **59**(1): p. 1-152.
24. Hozumi, A., et al., *Fluoroalkylsilane Monolayers Formed by Chemical Vapor Surface Modification on Hydroxylated Oxide Surfaces.* Langmuir, 1999. **15**(22): p. 7600-7604.
25. Raichur, A.M., X.H. Wang, and B.K. Parekh, *Quantifying pyrite surface oxidation kinetics by contact angle measurements.* Colloids and Surfaces A: Physicochemical and Engineering Aspects, 2000. **167**(3): p. 245-251.
26. Okrusch, M. and S. Matthes, *Mineralogie: Eine Einführung in die spezielle Mineralogie, Petrologie und Lagerstättenkunde*. 2013: Springer Berlin Heidelberg.